Materials & Design 249 (2025) 113479

Contents lists available at ScienceDirect

Materials & Design

journal homepage: www.elsevier.com/locate/matdes

Prototyping high-fidelity multifunctional objects using single-nozzle multi-filament additive manufacturing system with active mixing

Teng Teng [a], Yefan Zhi [a], Masoud Akbarzadeh [a,b,*]

[a] Polyhedral Structures Laboratory, School of Design, University of Pennsylvania, Philadelphia, USA
[b] General Robotic, Automation, Sensing and Perception (GRASP) Lab, School of Engineering and Applied Science, University of Pennsylvania, Philadelphia, USA

ARTICLE INFO

Keywords:
Multimaterial additive manufacturing
Active mixing
Printer development
Functionally graded material
High fidelity printing

ABSTRACT

This paper aims to advance the field of additive manufacturing by producing multimaterial objects with intricate topological features and polylithic material distribution through an integrated approach. First, we develop a Single-Nozzle Multi-Filament (SNMF) system equipped with active mixing to blend multiple filaments and deposit a programmable mixture. The system can also deposit gradient transitions between different materials within a single print. Second, we establish a numerical model to represent the material transitional behavior and validated it with experiments. The model enables the precise control of the material transitional interface to ensure high material fidelity. Third, we propose three strategies for designing and modeling multimaterial objects catering to different application scenarios, including image sampling, 2D discrete patches, and 3D surface division. The system's capabilities were validated through six case studies designed and fabricated through the above approaches for distinct application scenarios, demonstrating the successful materialization of complex designs with multiple functionalities.

1. Introduction

1.1. Background

In 2016, MacDonald and Wicker [1] suggested that additive manufacturing (AM) devices could integrate multiple functions into a single object, with multimaterial additive manufacturing (MMAM) as a viable approach.

MMAM enables the deposition of distinct materials in specific locations within an object to achieve desired functions, evolving since the 1990s [2,3]. MMAM research surged post-2017, with over 200 publications by 2023. However, review articles by Nazir et al. [4], Li et al. [5], and Rafiee et al. [6] highlight persistent challenges, particularly the limited real-world applications beyond experimental studies. Nazir et al. [4] observed that most research focuses on characterization and performance analysis rather than application-specific MMAM processes.

For MMAM to advance practically, it must support complex topologies and diverse material compositions. Complex engineering applications, as noted by Gibson et al. [7], require components that withstand various stresses and thermal conditions. While single-material AM technologies allow intricate topologies [8,9], MMAM remains less developed in this area. Some, like Feng et al. [10], have used single-material printing and multimaterial assembly to achieve complexity.

To address multifunctional needs, MMAM must place materials precisely in regions to provide both structural complexity and localized properties. While composites offer multifunctionality, they lack optimal material distribution tailored to specific conditions [11]. Although MMAM has theoretical potential for such distributions, most studies prioritize material characterization over methods for enhancing material distribution in intricate structures.

1.2. Literature review

1.2.1. Technology development of extrusion-based MMAM

While most MMAM research focuses on empirically analyzing the characterization, properties, and performance of MM objects, relatively few studies emphasize the development of MMAM technology and the relationship between the manufacturing process and the performance of

Abbreviations: AM, Additive manufacturing; FDM, Fused deposition modeling; FFF, Fused filament fabrication; MM, multimaterial; MMAM, multimaterial additive manufacturing; PLA, Polylactic acid; PETG, Polyethylene terephthalate glycol; SNMF, Single-Nozzle Multi-Filament; TPU, Thermoplastic polyurethane; NEMA, National Electrical Manufacturers Association.

* Corresponding author at: Polyhedral Structures Laboratory, School of Design, University of Pennsylvania, Philadelphia, USA.
E-mail addresses: tteng@design.upenn.edu (T. Teng), yefanzhi@design.upenn.edu (Y. Zhi), masouda@design.upenn.edu (M. Akbarzadeh).

https://doi.org/10.1016/j.matdes.2024.113479
Received 24 September 2024; Received in revised form 7 November 2024; Accepted 18 November 2024
Available online 10 December 2024

printed objects. Nazir et al. [4] noted that MM objects often exhibit superior mechanical properties compared to single-material objects. However, Lopes et al. [12] emphasized that the mechanical performance of printed MM objects heavily depends on the material extrusion process and setup.

There are two primary material extrusion setups in MMAM: multi-nozzle and single-nozzle configurations. Multi-nozzle systems use parallel nozzles to deposit different materials during printing and are favored in many studies due to their ease of assembly [13–17]. However, these setups often result in discernible interfaces between materials, compromising bonding strength [18]. Additionally, switching between nozzles during the manufacturing process, along with the required system calibration, increases processing time [19–21].

Single-nozzle systems, on the other hand, use one nozzle to deposit multiple materials. In microfluidics fabrication, studies using low-viscosity polymers [21–28] have successfully produced MM objects at small scales with fine resolution using single-nozzle printheads. This continuous extrusion can enhance the performance of MM objects, as Baca et al. [29] reported, creating superior bonding between distinct materials compared to multi-nozzle configurations. Additionally, FFF-based studies [30,31] demonstrated that single nozzles could simultaneously extrude multiple materials into a continuous extrudate.

However, the improvements associated with single-nozzle setups are not universally consistent. Fenollosa et al. [31] pointed out that while the composition of the extrudate can be regulated, achieving a homogeneous mixture remains challenging. Cameron et al. [32] also reported that single-nozzle systems might compromise geometric integrity, leading to discontinuity and heterogeneous material blending in the printed extrudate. Tian et al.'s work [33] relies on a passive approach with a single nozzle, switching between different materials rather than mixing them in real-time. This system does not process gradient materials either, as its focus is on alternating between distinct materials rather than dynamically blending them. Lee et al.'s work [34] focuses on switching between different inks via a Y-junction nozzle, but without dynamically mixing them. As a result, it is not designed to process gradient materials. The scale of this approach is suitable for small to medium-sized food objects. Additionally, Baca et al. [29] found that while single-nozzle systems produced more consistent printed objects in thermoplastic filament printing, the overall structural strength improvement was minimal, less than 5 %.

To enhance material mixing in MMAM, particularly in extrusion processes, both active and passive blending elements can be employed [35,36].

Active mixing, involving a mechanically controlled blending element during printing, can accurately place diverse material mixtures across layers, facilitating seamless material transitions [29,37–41]. The key component, a controllable spinning screw inside the nozzle, mixes materials into a consistent blend and deposits them through shear force. Hassan et al. [42] created a system that employs a hybrid approach that includes both active and passive micromixing. This allows it to dynamically mix inks in real time, making it suitable for processing gradient materials. However, the system is only capable of printing at small scale. Kennedy et al. [43] demonstrated that active mixing ensures uniform material integration throughout the printing process. However, extrusion-based MM printers with active mixing are not yet commercially available, necessitating additional effort in printer development for high-performance MMAM investigations.

Although Nazir et al. [4] reviewed MMAM studies from 2017 to 2023, only a small portion detail the development of MMAM devices [30,44,37,45,46]. Song et al. [30] and Jaksa et al. [44] described developing single-nozzle material extrusion MMAM printers, though without active mixing features. Lan [37] integrated an active mixing nozzle into a material jetting printer, focusing on numerical modeling and simulation. Pelz et al.[45] used a single-nozzle setup with an active auger for mixing and extruding ceramics, enabling real-time material composition regulation. However, these projects disclosed limited details on system design and development. Most documented developments are related to multi-nozzle systems, such as Roach et al.'s M4 3D printer [46].

In conclusion, the field of single-nozzle MMAM extrusion devices with active mixing mechanisms requires a systematic development.

1.2.2. *Material fidelity of MMAM*

Current MMAM research predominantly focuses on characterizing the properties and bonding performances of MM objects, with less attention given to improving material fidelity. In traditional single-material additive manufacturing, the quality of printed objects is typically evaluated based on shape fidelity and dimensional accuracy [47]. Shape fidelity qualitatively assesses deviations from the original design's geometric features, including topology, morphology, details, and textures [48]. Dimensional accuracy quantitatively measures how closely the object's dimensions align with the design specifications [49]. The quality of printing is influenced by factors such as device precision, component suitability, material selection, and printing settings like nozzle size and layer height [47]. For instance, using a smaller nozzle size and finer layer height enhances dimensional accuracy [50], while the choice of printing method and material retention ability affects shape fidelity [51].

However, in the context of MMAM, the concept of printing quality needs to be broadened. Beyond shape fidelity and dimensional accuracy, the precision of material composition and distribution becomes crucial. We define material fidelity as the degree to which the material composition and distribution in the printed object match the original design.

Material fidelity is significant depending on the application of the printed MM object. High levels of material fidelity are essential for functional MM parts intended for assembly.

Producing MM objects with higher material fidelity contributes to increased complexity, thereby enhancing functionality. Complexity in multi-material printed objects refers to the intricacy of the object's structural topology and material distribution. Structural topology concerns the geometric arrangement and connectivity of topological members within the object, ranging from simple to intricate forms. While traditional single-material AM has successfully produced objects with complex topologies [8,9], MMAM has yet to demonstrate significant progress in this area.

Complexity in material distribution is defined as the arrangement of different materials within the object. Less complex objects exhibit monolithic material compositions with continuous transitions, whereas more complex objects feature polylithic compositions with discrete material organization, often enabling distinct material properties in specific regions. Table 1 illustrates the definition of complexity within the MMAM perspective.

As reported in review articles such as [4–6,55–58], the field of MMAM places less concentration on MM object's fidelity improvement, and there are no cases that are able to print intricate topological structures with monolithic and polylithic material composition as shown in the graphical illustration of Table 1c and d. A handful of studies, such as Song et al. [30], Skylar-Scott et al. [17], Hardin et al. [26], and Uzel et al. [54], were able to print MM two-dimensional patterns and three-dimensional geometries with fine fidelity to reach to the polylithic material composition but only capable of forming relatively simple topology, as demonstrated in the graphical illustration of Table 1b.

The works above with high fidelity can further benefit from embedding active mixing to produce intricate topological structures with polylithic material composition, meeting the intended functionality as shown in Table 1d. Precedent works, such as [37,45,52], have demonstrated that MM extrusion with active mixing is capable of producing elementary geometry with monolithic material composition as shown in Table 1a. Green et al. [52], Lan et al. [37], and Ober et al. [40] enabled composition control on the fly with a single active mixing nozzle to fabricate geometries such as rings, cubes, cylinders, and tensile

Table 1
A graphical illustration of MM objects' complexity: (a) geometry designed with simple topology and monolithic material composition; (b) geometry designed with simple topology and polylithic material composition; (c) geometry designed with intricate topology with monolithic material composition; (d) geometry designed with intricate topology with polylithic material composition.

Simple topology		Intricate topology	
(a) Monolithic Material Composition	(b) Polylithic Material Composition	(c) Monolithic Material Composition	(d) Polylithic Material Composition
	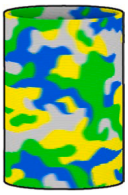		
Green et al. [52] Lan et al. [37] Pelz et al. [45] Ober et al. [40] Li et al. [53] Ducan et al. [41]	Song et al. [30] Skylar-Scott et al. [17] Hardin et al. [26] Uzel et al. [54]	No existing literature But can be achieved via the proposed technology and methodology.	No existing literature But can be achieved via the proposed technology and methodology.
w/ active mixing	w/o active mixing	w/ active mixing	w/ active mixing

specimens. Meanwhile, all samples are of monolithic material composition as shown in the graphical illustration Table 1a. Empowering the MMAM with high shape and material fidelity to produce an object with intricate topological structures and multiple gradient material distributions will satisfy the various demands of different applied fields and creative communities.

Yet, the limitation of active mixing embedded MMAM system is explicit. The incorporation of the blending element increases the complicity of the printing system. More factors related to the blending element need to be considered, including the compatibility between the hardware and the blending element, the controllability of the blending element, and the operational procedure of design and fabrication. Without systematic control over hardware, software, and design-to-fabrication workflow, the high fidelity of MMAM is infeasible, and the design, process, fabrication, and practical usage of multi-material products remain challenged.

Therefore, comprehensive control of active mixing for high-fidelity MMAM is needed.

1.2.3. Design and modeling for fabrication of complex MM object

In addition to the lack of disclosure development content regarding the MMAM system and limited fidelity with active mixing in the material extrusion system, it is reported that the design and modeling method of MM objects is scarce and limited [4]. Commercial slicing software, such as Ultimaker Cura and PrusaSlicer, while not designed to cope with design and modeling tasks naturally, also lacks the ability to incorporate distinct material information into machine instruction programs (e.g., G-code), resulting in subpar control over material composition on the fly. Yet, the current commercial CAD tools are targeting design instead of fabrication of MM objects. This limitation leads to the overall design of the MM object being unable to achieve relatively high complexity, both structural and material-wise, such as showed in the precedent research works [37,45,52,40]. However, when the MM objects are printed to be utilized functionally in an assembly, it is crucial for the MMAM to be incorporated with intricate topological structures and multiple gradient material distributions at the design and modeling stage. So that the fabrication process of the MM object can be well-guided and the final product can be expanded to broader application scenarios. Early attempts, such as Qiu and Langrana [59]and Bhashyam et al. [60], established standalone CAD tools to represent heterogeneous materials without engaging the manufacturing process. Wargnier et al. [61] and Yao et al. [62] both proposed a multimaterial object design framework that assists users in the multimaterial assignment, selection, and manufacturing guidance. Yet, Wargnier et al. [61]'s proposal is merely theoretical without toolkits being developed. Yao et al. [62]'s operations didn't target building intricate topological structures. Wade et al.'s OpenVCAD [63] developed a volumetric-based workflow to produce a multimaterial toolpath for material jetting printers. Nonetheless, more printing validations for these slicing tools and workflow are needed when working with specific devices. To materialize the MM object with higher topological and material complexity, the development of a new design-fabrication strategy is necessary.

1.3. Motivation and objectives

We aim to additively manufacture multimaterial objects with both intricate topological features and polylithic material compositions. It is essential to adopt a holistic approach that systematically incorporates different aspects of MMAM. The mentioned gaps regarding the lack of material extrusion technology development literature, comprehensive methodology to control the active mixing for higher fidelity, and proper design/modeling strategy for intricate MM objects highlight the potential for continued research and development in this area. From a material extrusion perspective, our research intends to fill the gap in active mixing embedded single-nozzle multimaterial extrusion systems for high-fidelity MMAM production. Taking the FFF process as a case study, the research's contribution to MMAM is threefold.

First, a robust printing system setup, including a hardware design capable of handling multiple materials simultaneously. Meanwhile, the system implementation supports intricate numerical control over the multiple material-feeding elements and can be programmed based on the demand for the designed application. The 2.1 section in our research debriefs a developed and fully functional Single-Nozzle Multi-Filament (SNMF) system that features an active mixing mechanism. The active mixing mechanism, while ensuring performance improvement on the printed object, enables the production of MM objects with gradient composition and transitions. The section details the design and engineering of the hardware and electrical system. It also reports the numerical model established for system control. The information documented here patches the missing information of the MMAM research realm and provides more options for interested readers to develop capable MMAM devices.

Second, it requires a deep understanding of material transitional behavior—how materials behave when switching during the printing process—to avoid defects and ensure that the final object meets its design specifications for achieving high material fidelity. The 2.1 section in our research offers a comprehensive methodology for the full control of active mixing to achieve higher fidelity. The methodology allows users to compose numerical control (NC) programming language, namely the G-Code, with embedded material information for multi-material production. Specifically, investigating material transitional behavior enables the accurate placement of various materials by eliminating the transitional delay caused during material switching; hence, dispensing multiple materials at the same printing layers to achieve multiple gradient material distributions is feasible. The investigation of gradient composition control allows the system to regulate various mixtures of materials in the designed composition. These efforts ensure high-fidelity printing of MM objects, therefore enabling the opportunity to achieve higher complexity to satisfy the demand of practical applications.

Third, In addition to these technical components, advanced design and modeling strategies are crucial for efficiently creating multimaterial objects tailored for different application scenarios. Strategies must be developed that allow designers to model objects with intricate

topologies and carefully controlled material distributions. These strategies should enable the creation of both monolithic and polylithic material compositions, ensuring that the final printed objects exhibit the desired functional properties across their entire structure. In the result section 3.3, we debrief three practical design and modeling strategies for generating MM objects. The outcome of these strategies is showcased with various printed objects for different fabrication scenarios, including multiple gradient material distributions, 2D patterns, and 3D geometry with intricate structure and material distribution. The strategies are compatible with our system, utilize conventional Computer-Aided Design(CAD) software, and produce fabrication-ready documents embedded with accurate and differentiated material information to deliver high-quality MM objects.

2. Methodology

This section outlines the integrated approach to materialize the MM object with intricate topological features and polylithic material distribution from three aspects. The hardware design and engineering session briefs the working principle of designing a single-nozzle MM 3D printing system and the system implementation. The multimaterial extrusion test describes the programmable composition control of the mixture and transitional behavior during the transition period of material deposition. The design and modeling strategies illustrate methods to create digital representations of designed MM objects and convert them into print-ready G-code for MMAM.

2.1. System setup

Printhead Design. The conventional DFM printer inspires the printhead design in this research. Fig. 1a shows a typical single filament desktop 3d printer consisting of three key components: a material supplier feeding the filament, a printhead for extruding semisolid material, and a numerically controlled motion platform (a gantry or robotic arm). These components work together to control material deposition according to a designed pattern. Fig. 1b is the multimaterial scheme of "Diamond Hotend", designed by RepRap online community [64] and tested in [29]. A similar design has also been used in Song's work [30]. It features multiple input filaments merging into one output nozzle. However, the design without a blending mechanism may result in clogging issues that cause extrusion discontinuity and poor filament bonding. Fig. 1c is the proposed Single-Nozzle Multi-Filament (SNMF) printing system, which modifies the typical desktop 3d printer and Diamond Hotend.

The Fig. 1c's configuration is initially established based on the number of filaments needed. Each filament requires an individual filament supplier motor to be transported through the Teflon hose. The filaments are then melted under a certain temperature and extruded. When switching the filament, the auger embedded in the nozzle blends the two filaments, creating a transitional segment in the deposited extrusion. The blending process can also create gradient material mixtures when multiple filaments are fed in a designed composition, which will be further discussed in the section 2.1. The detailed information regarding the system setup and configuration change can be found in the Supplementary Information.

Numerical Control. The motor control scheme is developed based on the following equations. In a single-filament system, the feeding motor's linear speed v is

$$v = \frac{Q}{\pi d^2/4} \tag{1}$$

where Q is the desired volumetric flow rate, and d is the diameter of the filament. Empirical tests have been conducted to find the directly proportional relation between Q and the auger rotation speed ω so that filaments can be extruded consistently without over/under-pressurization,

$$\omega = \frac{Q}{Q_0} \times 1\text{RPS} \tag{2}$$

Q_0 is the observed material flow rate when the auger runs at 1 RPS (revolution per second). In a multi-filament extrusion system with gradient composition, the feeding motor linear speed of the ith filament is

$$v_i = p_i v \tag{3}$$

where p_i is the desired percentage of the ith filament. The section 2.1 will discuss the gradient composition of filaments to form different materials and the determination of filament deposition percentages. Table 2 gives a nomenclature of the variables discussed.

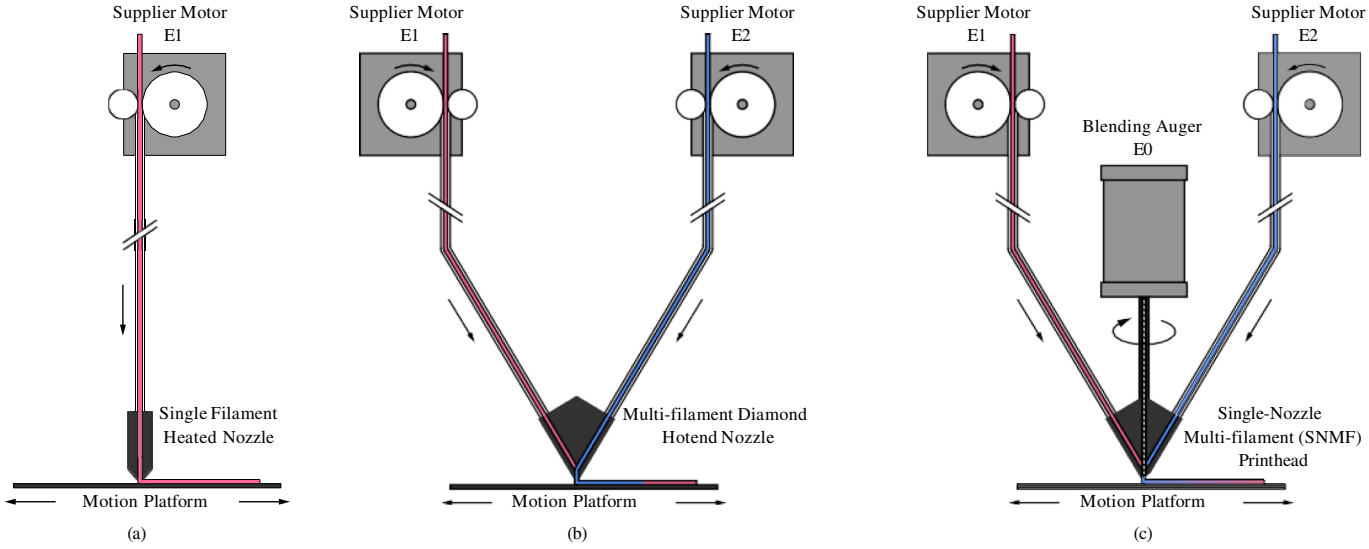

Fig. 1. The schismatic development of SNMF printing schemes: (a) the typical single filament printer, which is composed of a supplier motor, a heated nozzle, and a motion platform; (b) the multi-filament Diamond Hotend printhead designed by [64], in which multiple supplier motors feed multiple filaments; and (c) the proposed SNMF printer with a 2 mm screw drill embedded. Multiple supplier motors feed filaments into the single nozzle printhead, and the embedded 2 mm screw drill blends the filaments into a mixture based on the designed composition.

Table 2
Nomenclature for the symbols used in numerical control of the system.

Symbol	Unit	Description
Input		
Q	$mm^3\ s^{-1}$	Desired volumetric flow rate
d	mm	Diameter of the filaments
$_i$		Desired percentage of the ith filament
Output		
ω	RPS	Desired auger rotation speed
Q_0	$mm^3\ s^{-1}$	Volumetric flow rate when $\omega = 1$RPS
v	$mm\ s^{-1}$	Total linear speed of the supplier motors
v_i	$mm\ s^{-1}$	Linear speed of the ith supplier motor

The built SNMF system uses a maximum of four filaments and requires four material-feeding motors. In addition, three motors control the axes of the printbed and gantry, and one controls the blending auger.

The parameters of stepper motors, such as steps and current on stepper drivers, were set. The rotational speed of motors is adjusted in real-time by following the material profiles stored in G-Codes. Material profiles will be detailed in the section 2.1.

Finally, firmware modifications were made using Marlin 2.1.2 to enable mixing extruder functionality, allowing adjustments in motor speeds and facilitating smooth material transitions. This involves enabling the MIXING_EXTRUDER directive, specifying the number of steppers via MIXING_STEPPERS, and creating virtual tools for predefined mixing ratios.

System Implementation. The SNMF system prints multi-filament toolpaths using customized G-Code definitions. Modifying firmware allows M163 and M164 G-Code commands to be set up, and settings are saved for each filament. The process involves activating a specific filament with a regulated flow rate for extrusion and deactivat-ing the others, then saving this as a material configuration. This is repeated for each filament used in the printing.

The stored material configurations are sequentially recalled using the T command during printing. Then, the printhead moves to the appropriate coordinates and extrudes the selected filament at a predetermined flow rate, adhering to the specified toolpaths. This approach allows the switch between different filaments during printing.

Table 3 details the core G-Code commands and their roles in multimaterial printing. Fig. 2 shows how the gcode file sequentially make use of them.

Supplementary Information A.1. gives a sample code to print a continuous line with white (fil1), green (fil_2), and blue (fil_3) PLA filaments. Each segment of the toolpath curve is associated with a material configuration of a separate filament (white-T0, green-T1, blue-T2). Fig. 3 results from printing this code. It exhibits a seamless gradient transition due to extrusion with a blending auger.

The research uses an in-house developed software to turn curves with material information into G-Codes tailored for the SNFM setup.

2.2. Multimaterial extrusion of higher material fidelity

We argued that material fidelity is a crucial index for evaluating the quality of MMAM. Material fidelity is defined as the magnitude of material composition and distribution in the printed object that matches the original design. To address this, we propose two numerical methods

Table 3
Description of G-Code commands, lowercase letters are values to fill in.

Command	Description
M163 Ss Pp	Set the weight of extruder motor s to p
M164 Ss	Store the current mix as tool index s*
Tx	Select the previously stored tool index x

* $s = 0$ is the blending auger motor, which always weights 1.

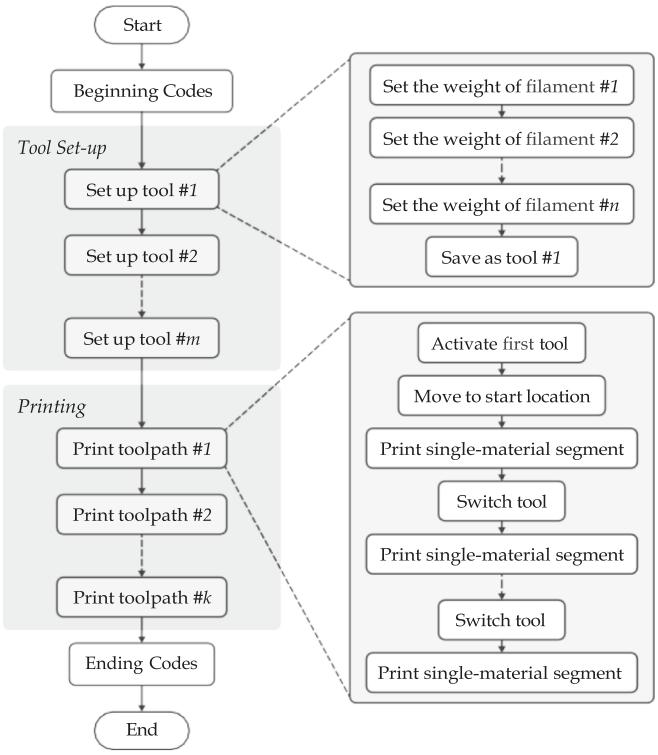

Fig. 2. Multimaterial G-Code flowchart.

to facilitate material fidelity, one of which enables programmable material composition, and the other permits more accurate material distribution.

Gradient Composition Control. The SNMF system can blend two or more filaments into a new mixture based on the designed material composition. Each mixture referred to as a *material profile* (or simply *material* instead of *filament*) in this article is a particular mixture of filaments defined by a series of numbers $p_1, p_2, \ldots, p_n$ specifying the percentage of each filament. In the case of black and white filaments, each material profile is a different grayscale color formed by blending the two in a certain proportion. More generally, when we can have m material profiles over n filaments, the profiles are stored in the in-house slicing software as a $m \times n$ matrix

$$P = \begin{matrix} mat_1 \\ mat_2 \\ \vdots \\ mat_m \end{matrix} \begin{pmatrix} fil_1 & fil_2 & \cdots & fil_n \\ p_{11} & p_{12} & p_{21} & p_{1n} \\ p_{21} & p_{22} & p_{21} & p_{2n} \\ \vdots & \vdots & \vdots & \vdots \\ p_{m1} & p_{m2} & \cdots & p_{mn} \end{pmatrix} \tag{4}$$

where $p_{i\,j}$ is the percentage of jth filament in ith material profile. In the example of Fig. 9,

$$P = \begin{matrix} mat_1 \\ mat_2 \\ mat_3 \\ mat_4 \end{matrix} \begin{pmatrix} fil_1 & fil_2 \\ 1 & 0 \\ 0.7 & 0.3 \\ 0.3 & 0.7 \\ 0 & 1 \end{pmatrix} \tag{5}$$

When printing multiple filaments without mixing them, as is the case of SI, **P** is an identity matrix:

$$P = \begin{matrix} mat_1 \\ mat_2 \\ mat_3 \end{matrix} \begin{pmatrix} fil_1 & fil_2 & fil_3 \\ 1 & 0 & 0 \\ 0 & 1 & 0 \\ 0 & 0 & 1 \end{pmatrix} \tag{6}$$

The speed of the filament supplier motors dominates the composition of the mixture. The required calculation is shown in Section 2.1. The

Fig. 3. The sample print of a continuous line with three segments of different colors.

sample code in SI illustrates the setup of ten material configurations over two filaments, defined as

$$P = \begin{matrix} mat_1 \\ mat_2 \\ \vdots \\ mat_{10} \end{matrix} \begin{pmatrix} fil_1 & fil_2 \\ 1 & 0 \\ 0.9 & 0.1 \\ \vdots & \vdots \\ 0.1 & 0.9 \end{pmatrix} \tag{7}$$

Material Transitional Behavior. The material transition starts when the nozzle reaches a *breakpoint* where material switches. The motor speeds change at the breakpoint. When switching from 100 % filament 1 to 100 % filament 2, motor E1 stops, and motor E2 starts. Filament 2 enters the mixing chamber in the nozzle and starts to push out residual filament 1. The material transition does not create a distinct interface at the breakpoint for two reasons: the new material has to travel through the nozzle, so there is a delay in transition; for a short period, the blending auger mixes and extrudes both materials until there is no residual old material, resulting in a gradient transition. Thus, this section aims to study these two behaviors empirically and interpret them with a mathematical approximation. To differentiate, the location where the motor starts to switch materials is referred to as the *motor breakpoint*, and the location of the observed interface is referred to as the *visual breakpoint*.

Fig. 4 illustrates a series of experiments to examine the material transitional behavior. A 200 × 50 mm 2D zig-zag toolpath is designed with a print section of 2 × 0.8 mm whose desired breakpoints are aligned in the middle (Fig. 4a) and used as motor breakpoints which are the inputs to the G-Code. The printing result (Fig. 4b) shows the mismatch between motor breakpoints and visual breakpoints caused by the delay. The motor breakpoints are moved backward by *advancement length L* to align the visual breakpoints. The motors are instructed to switch before they reach the desired breakpoint by trying different advancement lengths (Fig. 4d, e, g, and h), a fixed $L = L_0 = 18$ mm is associated with the material and design configuration. It reflects the distance between the motor breakpoint and the visual breakpoint.

When the overall extrusion rate (the rotational speed of the blending auger) is fixed, and the materials have the same or similar viscosity, the delay, and transition should take constant volumes in each switch. When the extruding section area is fixed, they take constant length. Fig. 5 interprets the material transitional behavior from 100 % filament 1 to 100 % filament 2 if the motor breakpoint is at x_0. The *delay length* L_1 is defined as the length from the motor breakpoint (x_0) to where the new filament starts to appear (x_1). The *transitional length* L_2 is defined as the length from where the new filament starts to appear (x_1) to where the old filament completely disappears (x_3). The test prints also measure the two values (Fig. 5a). While the mix-and-extrude process in the auger chamber is hard to depict numerically, we assume a linear composition change in the transitional length L_2. As reflected in

Fig. 5b and c, filament i's actual material percentage $R_i(x)$ at travel length x is:

$$R_i(x) = \begin{cases} p_i, & if x < x_0 + L_1; \\ p_i + \dfrac{x - (x_0 + L_1)}{L_2}\left(p_i' - p_i\right), & if x_0 + L_1 \leqslant x < x_0 + L_1 + L_2 \\ p_i' & if \} x \geqslant x_0 + L_1 + L_2. \end{cases} \tag{8}$$

if the motor breakpoint is x_0 and the desired composition changes from p_i to p'. In our approximation, the midpoint of the transition segment ($x_2 = x_0 + L_1 + {}^1L_2$) where $R_1(x) = R_2(x) = 0.5$ is regarded as the visual breakpoint. This means the visual breakpoint is delayed by:

$$L_0 = L_1 + \frac{1}{2}L_2 \tag{9}$$

and our measurements of the three values should match this expression. Therefore, before the G-Code is generated, the breakpoint is moved backward by L_0 so the supplier motors are switched in advance.

The relation in Eq. (8) can be further generalized using a moving average filter:

$$R_i(x) = \frac{1}{L_2}\int_{x-(L_1+L_2)}^{x-L_1} p_i(x)dx \tag{10}$$

where $p_i(x)$ is the desired material percentage or relative motor speed of filament i at travel length x. Eq. (10) results in the same curve in Fig. 5c. The benefit of formulating it as a moving average is that, unlike Eq. (8), Eq.

(10) is a generalized method applicable to any number of materials and rapid switches whose intervals are less than the transitional length L_2. With this expression, the in-house slicing software visualizes any design before printing to check the effects of different materials and

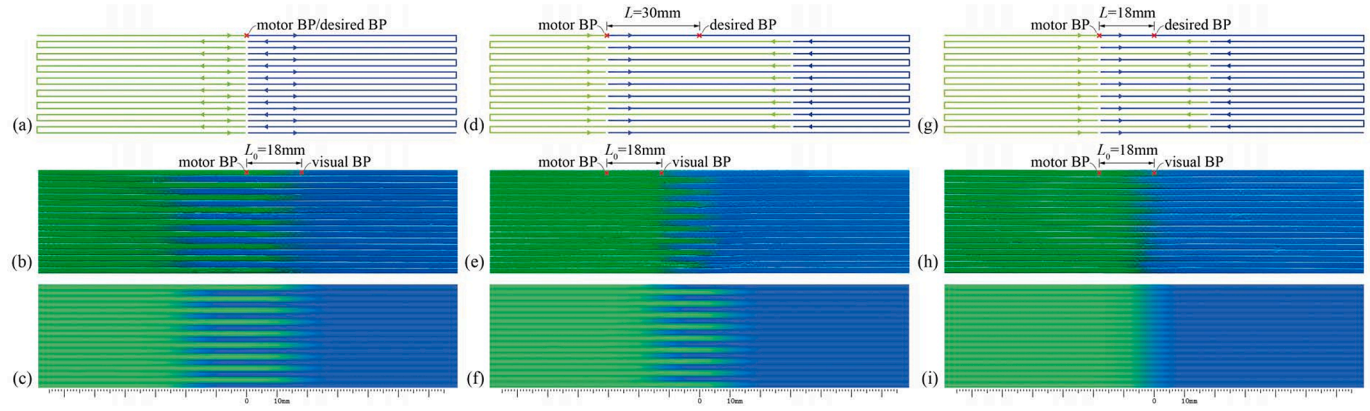

Fig. 4. Material transition tests of black and white PLA showing different breakpoints (BP). Toolpaths, print results, and visualization of prints with: (a) (b) (c) no advancement; (d) (e) (f) advancement length $L = 30$ mm; and (g) (h) (i) advancement length $L = 18$ mm. The visualizations (c) (f) (i) are generated after the tests are done, and the total mismatch between motor and visual breakpoints L_0 is solved.

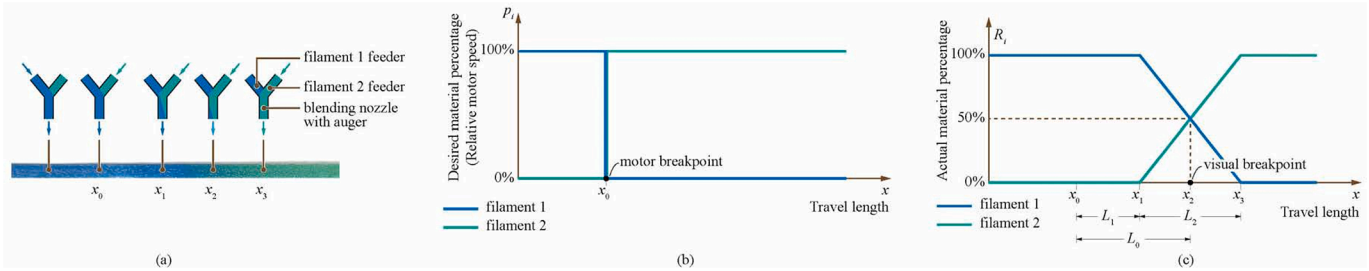

Fig. 5. Mathematical interpretation of material transitional behavior: (a) blending and print condition; (b) the relative speed of each filament's feeding motors; and (c) the actual percentage of each material in the print.

toolpaths, as shown in Fig. 4 and other examples in this article.

2.3. Design and modeling strategies

Here, we briefly provide three strategies for designing and modeling MM objects to generate material-informed toolpathing. We will discuss them in detail in Section 3.3. The strategies suggest different automatic and practical approaches but are not mutually exclusive in essence.

Multimaterial Printing via Image Sampling. The simplest way to approach multimaterial printing is to start with an image, as depicted in Fig. 9. We break down an infill pattern into small segments, sampling their colors directly from the image. These segments act like pixels, piecing together to form the complete image. This technique, especially when applied to images from CT scans and MRI results, can pave the way for new applications.

The process begins with selecting an image and converting it into a monochrome bitmap. We then extract the grayscale value from each pixel. Considering the extensive number of pixels, we adopt a modular approach based on these grayscale values. This involves categorizing the grayscale into several intervals.

We assign each pixel to a grayscale interval based on its value, averaging the values within each interval. Subsequently, we match the average grayscale of each segment to a specific blending ratio for multimaterial 3D printing.

As the printer's extruder follows its path, crossing areas mapped to specific grayscale modules, it adjusts the material blend in real time according to the preset ratios. This precise adjustment during printing ensures the material composition accurately reflects the desired output.

Multimaterial Printing with Discrete Patches. Components fabricated via additive manufacturing methods often necessitate specific structural attributes to address the complex loading conditions within the overall structure. In many applications [65–67], the alteration of toolpath orientation can be employed to modulate the load-bearing capability of the printed component. Through the multimaterial printing system proposed herein, beyond merely adjusting toolpath orientation, we introduce a novel avenue for enhancing the mechanical performance of structural components, namely, utilizing materials with differing mechanical properties for printing. Materials resistant to tension are deposited on toolpath segments subjected to tensile forces, while materials resistant to compression are deposited on segments under compressive forces. At the interface of these divergent materials, a graded transition is employed to augment the bonding between materials, thereby holistically improving the mechanical performance of structural components. This printing methodology necessitates a material distribution based on loading conditions across different toolpath segment patches, concurrently embedding material information within the machine-executable G-code for printing operations. Utilizing a continuous toolpath for 3D printing offers significant advantages, such as reduced production time and enhanced material bonding, by mitigating issues of underfilling and overfilling [65].

Multimaterial Printing with Surface Division. Printing a shell in 3D is known as contour-crafting or surface printing. A surface can be divided and assigned with different materials to tailor its local properties. Figs. 12 and 13 are examples where stronger materials are assigned to the funicular members or the stress-concentrated areas to enhance structural performance under specified loading cases. The surface division can be done by sampling another object (FEA's results as in Fig. 13), a field, or using intersectors. Toolpath curves are sliced after surfaces are divided and annotated. With the help of a hierarchical data structure as in Chiu and Tan [68], this method can also be expanded to print geometries of intricate 3d topological structures, such as a shell with infill patterns.

Printing intricate 3d topological structures with a multimaterial approach is challenging as it is necessary to implement differentiated material's heterogeneous distribution both horizontally and vertically in a layer-by-layer manner. Beyond multimaterial printing discrete patches, we managed to print complex 3D morphology using the surface division method, which is more capable of handling complex material distribution. The surface division method utilizes external objects as an intersector to sample a particular area in the target geometry for assigning differentiated materials. The following case studies showcase converting a prior-designed geometry structure into a multimaterial piece.

3. Results

This session presents the results of three research objectives listed in 1.3 that the authors intend to address. An SNMF printer is built to be capable of printing multiple filaments through one nozzle simultaneously. An empirical study regarding how active mixing contributes to material fidelity is conducted based on the established numerical model of gradient composition control with multimaterial transition behavior. The study also utilized three design and modeling strategies to design and produce various types of geometry with discrete material distribution in a continuous manner.

3.1. Developed printer

The Fig. 1c's configuration is designed and engineered into a modular single-nozzle multi-material printhead, as illustrated in Fig. 6. This customized printhead features a 3D printed 4-in-1-out aluminum alloy nozzle connected to four sets of E3D V6 heatsink/heat throat assemblies. Each assembly is linked through a hose to its respective Titan extruder, driven by an individual material supplier stepper motor. The aluminum alloy nozzle is engineered with four input chambers that merge at the center and connect to a single output chamber. The dimensions of the output chamber are set at a 2-mm diameter and a 5-mm length, and the nozzle is fabricated using selective laser sintering of aluminum alloy powder.

A 2 mm diameter auger is embedded in the output chamber driven by a stepper motor to ensure the material extrusion's continuity and homogeneous mixture. The 4-in-1-out aluminum alloy nozzle also incorporates space for a 24 V, 70 W Ceramic Cartridge Heater and a 100 K NTC thermistor. This design feature facilitates a robust heating process

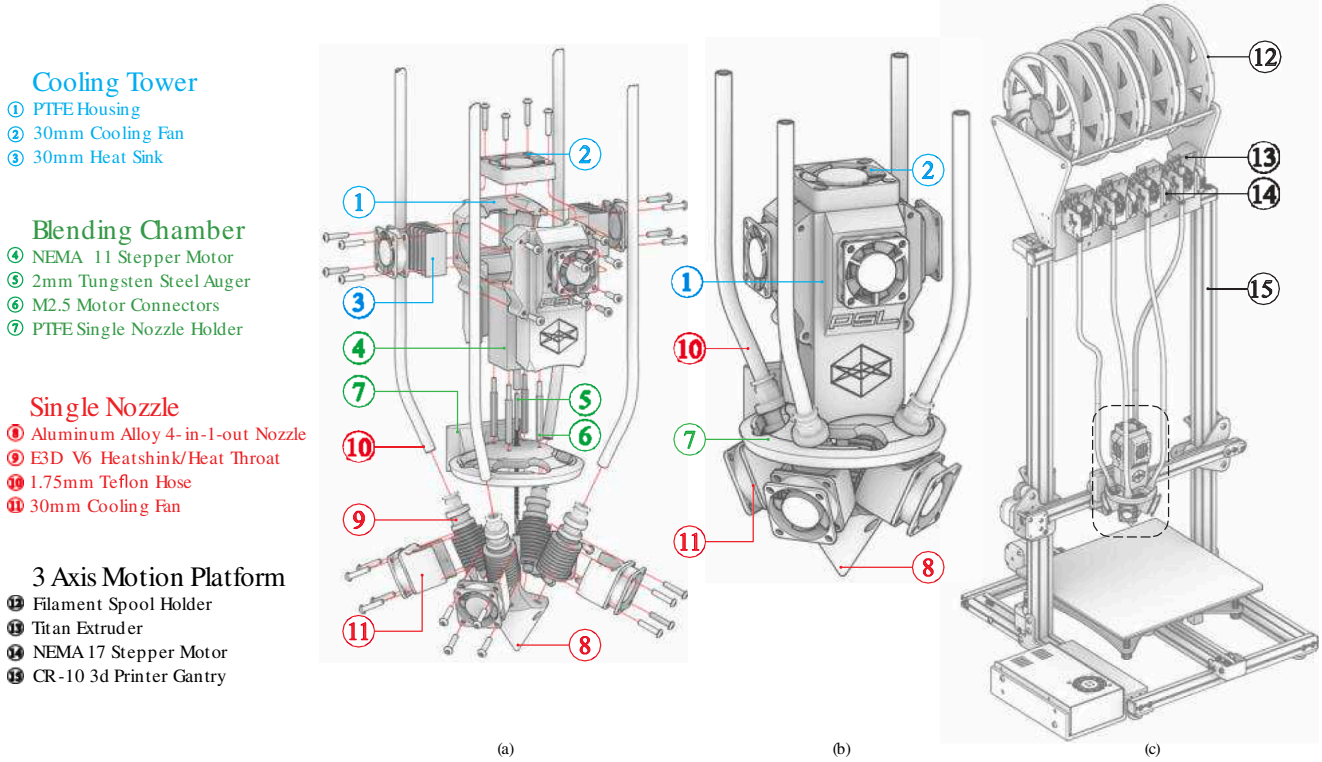

Fig. 6. Assembly and integration of an SNMF printhead for 3D Printing:(a) Disassembly diagram of an SNMF printhead, including a NEMA 17 stepper motor, a 2 mm tungsten steel auger, a PTFE single nozzle holder, and associated thermal management systems comprising a 30 mm cooling fan and heatsink apparatus; (b) Assembled view of the SNMF printhead. This assembly highlights the filament's path through the PTFE housing into the blending chamber, culminating at the single extrusion nozzle; (c) Installation schema of the printhead on a standard 3D printer framework, specifically the CR-10 gantry system. This schematic diagram details the printhead in situ, aligned with the 3-axis motion platform and equipped with a filament spool holder.

with Proportional-integral-derived (PID) control, ensuring reliable material melting and extrusion. Following the successful setup and experimentation with the Single-Nozzle Multi-Filament printer, to fully showcase the SNMF printer's capabilities, we conducted more tests of our system's performance in terms of con-trolling the material fidelity via active mixing element.

3.2. Validating performance of material fidelity

3.2.1. Gradient material composition

In the initial study in Sec 2.2, we establish the numerical control method in terms of gradient material composition and enable the transition between two colors of materials in a controlled manner.

Fig. 7 is the visualization and test printing result using this setup by having red and green PLA as the two filaments. To print the test piece that gradually transits from green PLA to red PLA, we used the above SNMF setup configurations with ten various material compositions embedded. The in-house slicing software generates the visualization with the color of the two filaments as input in Fig. 7a. Fig. 7b demonstrates the printed piece by mixing two filament's RGB channels according to the compositions to reflect the designd mixtures. The comparison in Fig. 7c shows how the colors of the actual mixture differ from the theoretical values in RGB format using the image processing method.

To measure the color deviation between the toolpath visualization and the printed sample, we extracted the average color intensity profiles for the red and green channels along the vertical axis of each image. By plotting these profiles, we compared the designed gradient (toolpath visualization) with the actual printed output.

The results in Fig. 7c revealed a general alignment in the designed and printed gradient composition but significant deviations in green and minor deviations in red in the initial section of the print. This deviation is likely due to inconsistencies in the material deposition or color mixing as the printer begins the gradient transition. While the printed sample's color intensity gradually aligns more closely with the toolpath in the middle and final sections, the initial green intensity is less stable, indicating a need for improved control over the material blending process, particularly the control over the active mixing element.

3.2.2. Material transitional behavior

To better understand the material transitional behavior, in addition to establishing the numerical method, we also conducted experiments to observe how the active mixing auger contributes to material gradient and transition.

First, two PLA filaments with different colors (red and blue) but similar viscosities were used to evaluate the effect of various auger rotational speeds on material transition and blending in an SNMF 3D printing setup. In Fig. 8a five test samples were printed with auger speeds set at 150, 125, 100, 75, and 50 rpm, transitioning from red to blue filament. Each sample was printed with a layer height of 0.8 mm and a width of 3 mm, with mixing and transition starting at a marked point. The use of filaments with similar viscosities helped ensure that observed differences in transition quality were primarily due to the auger speed rather than viscosity variations between materials. The results show that higher auger speeds (150 and 125 rpm) created sharper, more distinct transitions, facilitating rapid material changes but with minimal blending. This characteristic may be beneficial in applications that require clear material boundaries. A mid-range speed (100 rpm) displayed a moderate gradient, balancing transition smoothness with efficiency, suggesting it may be ideal for applications needing both smooth gradients and fast material changes. Lower speeds (75 and 50 rpm) produced the longest and smoothest transitions, with more gradual blending, making them suitable for applications prioritizing bonding strength and continuous gradients, though they may be less efficient for

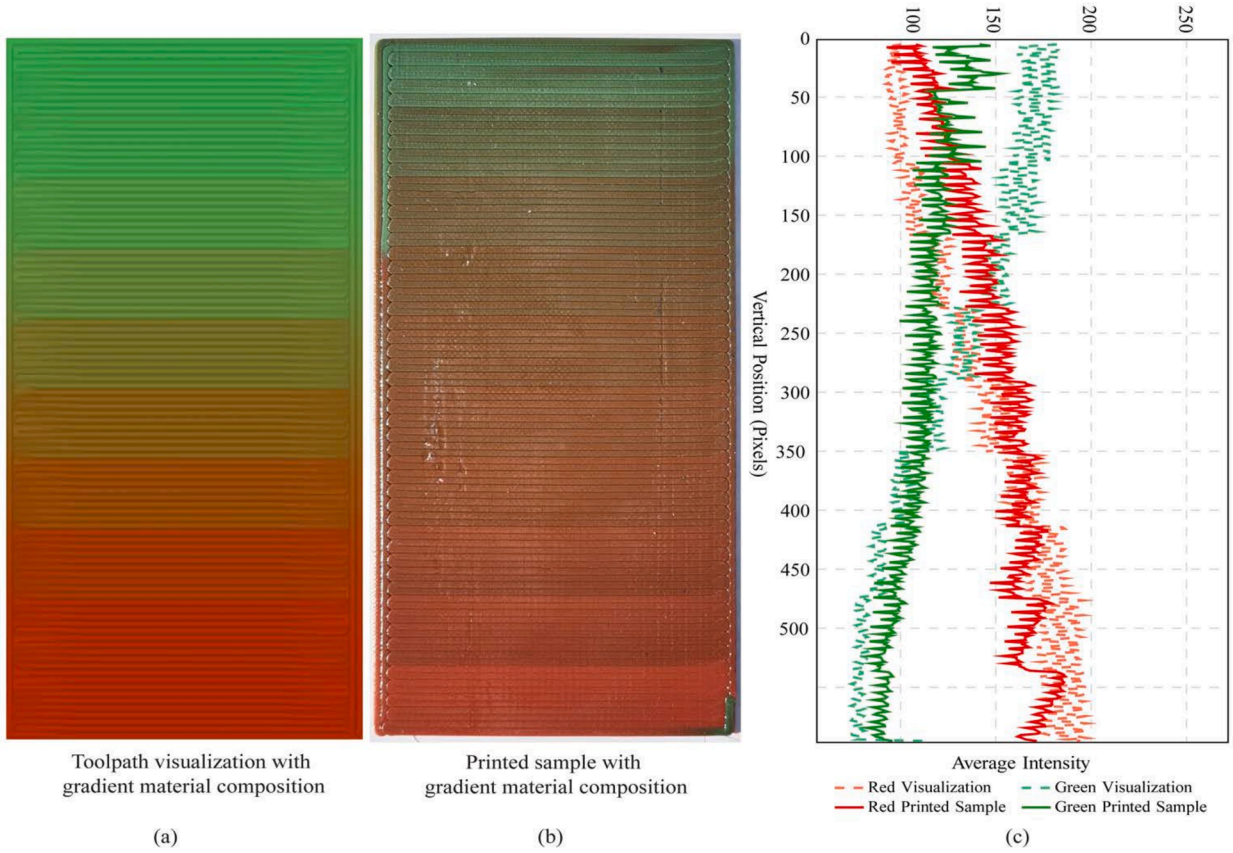

Fig. 7. Material composition test (200 × 100 mm) of 10 different mixtures using red and green PLA filaments: (a) visualization of the zig-zag toolpath with ten different material profiles, which is designed to be transiting from the mixture of 100 % red PLA/0% green PLA to the mixture of 10 % red PLA/90 % green PLA; (b) printed sample represent the same material composition design.(c) comparison between the actual color and theoretical color via image processing, a general alignment in the designed and printed gradient composition but deviations in the initial section of the print. (For interpretation of the references to color in this figure legend, the reader is referred to the web version of this article.)

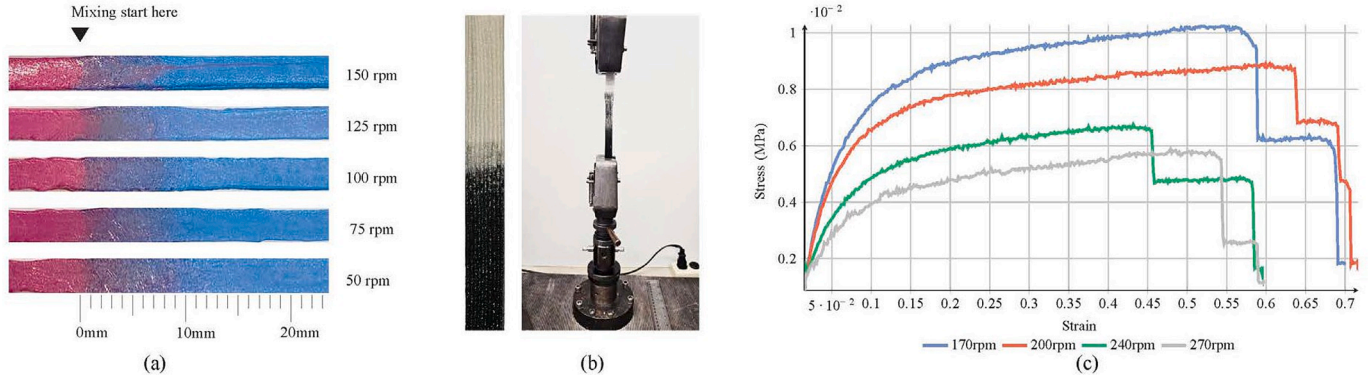

Fig. 8. (a) Samples printed with red and blue PLA filaments at different auger speeds (150, 125, 100, 75, and 50 rpm) show varying gradient lengths and blending qualities. Higher speeds produce sharper transitions with distinct boundaries, while lower speeds yield smoother, more gradual gradients. The mixing process begins at the marked point, with each sample printed at a layer height of 0.8 mm and width of 3 mm, (b) four 3D-printed strips were fabricated using white PLA transitioning to black TPU to examine the effects of different active mixing auger rotational speeds (170, 200, 240, 270 rpm) on material bonding, (c) the tensile test results indicating lower rotational speed results in higher bonding performance. (For interpretation of the references to color in this figure legend, the reader is referred to the web version of this article.)

rapid material changes. These observations suggest that lower speeds improve bonding and gradient smoothness, higher speeds provide distinct separations, and 100 RPM offers a balanced approach.

We also investigated the effects of active mixing auger rotational speeds on the bonding strength and stiffness of 3D-printed samples transitioning from distinct material, specifically from white PLA to black TPU. Due to the differing viscosities of PLA and TPU, achieving strong bonding between these materials is challenging, as reported in Brancewicz et al. [69] and Sorimpuk et al.'s works [70]. However, by controlling the rotational speed of the active mixing auger, we optimized the bonding strength at the interface. We printed 200 mm x 19 mm x 4 mm test strips with four different active mixing augers speeds, 170, 200, 240, and 270 rpm, and conducted tensile tests to evaluate the mechanical properties of each sample, as Fig. 8b.

The tensile test results in Fig. 8c indicate that lower rotational speeds (170 and 200 rpm) resulted in stronger bonds and greater stiffness, as shown by higher peak stress and initial slope in the stress–strain curves. Specifically, the sample printed at 170 rpm achieved the highest bonding strength, followed closely by the 200 rpm sample. These lower speeds allow for more thorough mixing at the interface, resulting in better material cohesion and structural integrity. In contrast, higher speeds (240 and 270 rpm) led to decreased bonding strength and stiffness, with lower peak stress values and more pronounced strain at failure. This suggests that higher speeds reduce mixing effectiveness, weakening the bond between PLA and TPU. These findings underscore that regulating the auger speed, particularly at lower settings, enhances bonding strength and structural performance in multimaterial prints with dissimilar viscosities.

3.3. Multimaterial printing case studies via various modeling strategies

3.3.1. Image sampling

Printing 2D Pattern from Image. To demonstrate our method's effectiveness, we chose Leonardo da Vinci's *Mona Lisa* in Fig. 9 as a test image. We processed the image into a bitmap and aimed to recreate it with multimaterial printing, maintaining its visual essence.

Using Adobe Photoshop, we converted the *Mona Lisa* into a grayscale bitmap. This conversion process quantized the image's grayscale values into four distinct levels (0, 0.3, 0.7, 1), as previously discussed in *Gradient Composition Control* in session 3.2. Each level corresponds to a predetermined material composition, allowing us to reproduce the grayscale through specific material compositions accurately. We also established a continuous zig-zag toolpath, with the spacing between paths matching the nozzle's diameter (2 mm) over a 12 × 12 cm area. In the G-code, we set four mixing ratios with the M163 and M164 commands, corresponding to the image's grayscale levels. We used black and white PLA filaments for the final print. The printer adjusts the blending ratio as it moves, depositing the material mix to achieve varied compositions.

This printing test highlights the capability of our system to replicate detailed 2D patterns through multimaterial printing.

3.3.2. Discrete patches

In the discrete patches implementation, multiple samples have been produced.

2D Structural Object. To evaluate the mechanical enhancement from our approach, we fabricated two Pratt truss samples (Fig. 10) for a three-point bending test. Each sample was printed with a 0.8 mm layer height, 2 mm extrusion width, and dimensions of 250 mm (length), 65 mm (height), and 16 mm (thickness), with each print taking about one hour. The experimental sample used HATCHBOX white PLA for compressive elements and OVERTURE Carbon Fiber reinforced PLA for tensile elements. The control sample was entirely printed with HATCHBOX white PLA. Both samples were printed at with a 30 mm/sec print speed. The multi-material specimen comprised 52.5 % tensile and 47.5 % compressive toolpath, weighing 166 g compared to the 179 g single-

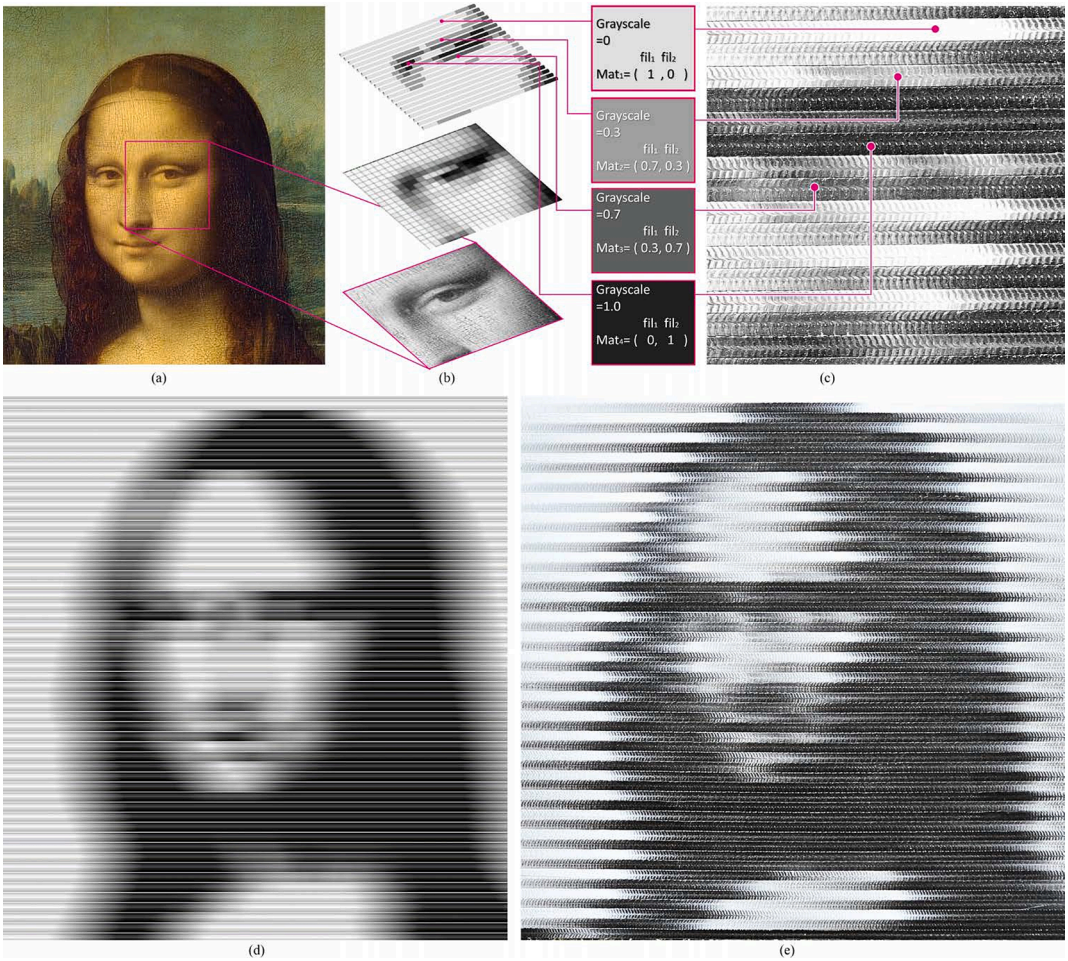

Fig. 9. Grayscale SNMF printing using black and white filaments. The toolpath is generated based on an image sampling of the *Mona Lisa* by Leonardo da Vinci: (a) the original *Mona Lisa* as input bitmap; (b) the monochromated bitmap sampled as pixels of four grayscales and reflected in the material-informed toolpath; (c) enlarged printed pattern showing different grayscales; (d) the toolpath visualization; (e) the final print using two filaments to produce the four grayscales.

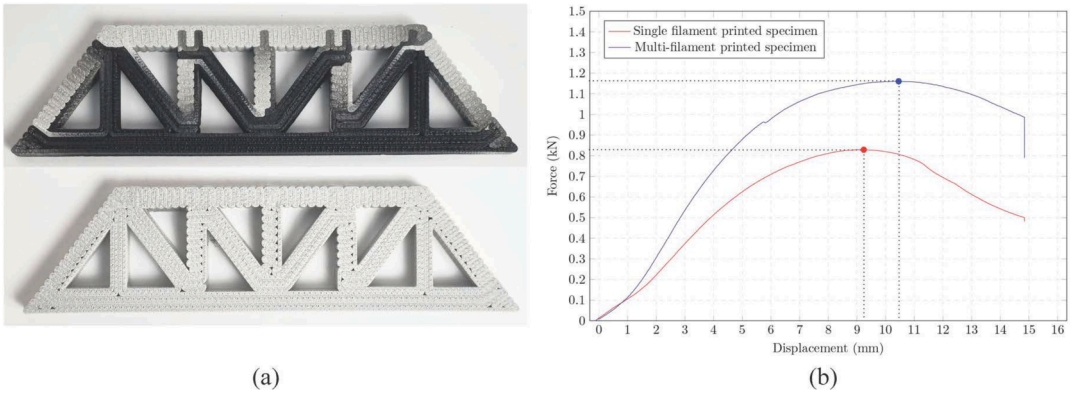

Fig. 10. (a) Two samples for the three-point bending test. Upper: multimaterial experimental specimen printed with HATCHBOX white PLA and OVERTURE Carbon Fiber reinforced PLA. Lower: single material control group specimen printed with HATCHBOX white PLA only. (b)Result of three-point bending test.

material control. The three-point bending tests were conducted using an Instron 4206 testing machine. The span length for the tests was established at 220 mm.

The three-point bending test was utilized to ascertain the maximal load that both specimens could endure. Fig. 10b reveals that the single-material control specimen succumbed to a load of 0.83 KN. In contrast, the multi-material experimental specimen withstood a load of up to 1.16 KN before yielding. At this juncture, one of the compressive members started to buckle, leading to overall plastic deformation within the truss structure. This outcome was anticipated, with the multi-material

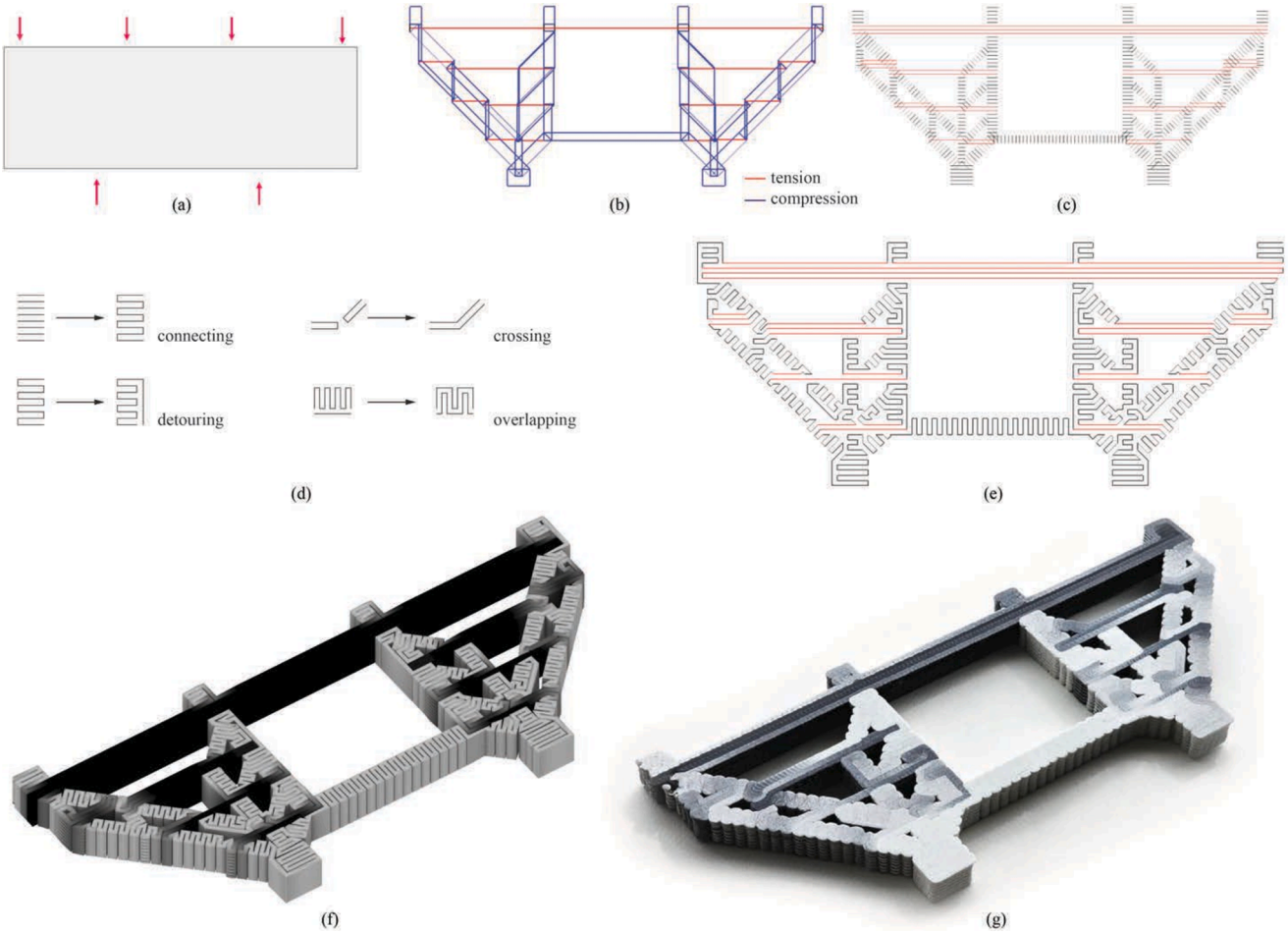

Fig. 11. SNMF printing of discrete patches. The toolpaths are generated based on the stress conditions over a strut-and-tie model: (a) the boundary condition for generating the strut-and-sie model with four loading points and two supports; (b) generated strut-and-tie model showing stress conditions using the method by [72]; (c) the color-coded raw toolpath curves aligned parallel to the direction of tension (red) and perpendicular to the direction of compression (black); (d) methods of connecting the raw toolpath curves for various scenarios; (e) the resultant global continuous path in which the red indicates the tensile members and the black indicates the compressive members; (f) the toolpath visualization, in which black indicates tensile members, white indicates compressive members, and (g) the final print uses carbon fiber-reinforced PETG filament for tensile areas and standard white PETG filament for the compressive areas. (For interpretation of the references to color in this figure legend, the reader is referred to the web version of this article.)

experimental specimen displaying superior stiffness compared to the single-material variant.

Additionally, Fig. 10b includes the load–displacement curves derived from the three-point bending tests of the respective specimens. These curves illustrate that the multi-material specimen exhibits significantly enhanced toughness compared to the single-material specimen. The area beneath the stress–strain curve quantifies toughness up to the fracture point. For our three-point bending test, the trapezoidal rule was applied for the numerical integration to calculate this area.

This numerical analysis indicated that the toughness of the multi-material sample is approximately 67 % greater than that of the single-material counterpart. The full method of generating this toolpath and performance enhancement through multimaterial printing is detailed in the previous study [71].

Intricate 2D Topological Structure. To further validate the proposed system's printability, we generated and printed an intricate 2D topological structure and a Pratt truss based on FEA from a three-point bending simulation. Using the algebraic graphic statics and layout optimization method [72], loading conditions (Fig. 11a) produced a strut-and-tie truss model reflecting tension and compression (Fig. 11b). Toolpaths were generated based on stress conditions, with tensile regions parallel and compressive regions perpendicular to stress directions (Fig. 11c). The toolpaths were post-processed into a global zig-zag path (Fig. 11e) for easier printing. Carbon fiber-reinforced PETG was used for tensile areas and white PETG for compressive areas. The visualization (Fig. 11f) closely matched the final print (Fig. 11g).

3.3.3. Surface division

We implemented two case studies using different approaches to showcase the surface division method for multimaterial printing.

3D Funicular Structure. The first approach transforms a pre-designed funicular structure into a continuous geometry using the SNMF printing system. Funicular structures, known for efficient force channeling, usually have segmented forms that complicate additive manufacturing due to toolpath discontinuities. Adding non-load-bearing material between these elements enhances functionality and simplifies printing by creating a continuous toolpath. The compression-dominated funicular polyhedral column in Fig. 12e was originally designed in 2018 [73] using the 3D Graphic Statics (3DGS) method. This parametric bar-node model allows adjustments to support positions, force magnitude, angle, and distribution while preserving the reciprocal relationship between form and force diagrams. The physical structure was created by casting concrete into a 3D-printed mold.

In the multimaterial iteration, we add mass between the interstitial spaces of the funicular members to create a continuum geometry. The original load-bearing capacity is preserved, while the added mass enables functions like insulation. As shown in Fig. 12, we use the original geometry as an intersector (a) to map material distribution on the continuum geometry. This geometry is then divided into two regions for different materials (b), sliced into multi-segment toolpaths with material information (c), and visualized for G-Code quality (d). The final print uses wood fiber-reinforced PLA for compressive members and lightweight foaming filament for insulation (f), retaining structural features with added insulation properties. Fig. 12g compares the original and new designs, showcasing the potential for functional enhancements using the Single-Nozzle Multi-Filament system.

3D FEA result of 3D Structure. The second approach converts finite element analysis (FEA) color codes into a physical model, aiding cross-

Fig. 12. SNMF printing of a funicular polyhedral column: (a) the base geometry (gray) and the intersector (brown); (b) divided surfaces; (c) multimaterial toolpath curves generated based on the surface division; (d) the toolpath visualization (layer height exaggerated for display); (e) the base geometry cast using concrete with a height of 250 mm in [73]; (f) the final print with a height of 250 mm; and (g) the comparison details of the two artifacts.

disciplinary understanding of structural behaviors and material requirements. Traditional multimaterial 3D printing often struggles to accurately represent detailed, color-coded FEA results withseamless transitions [74]. The proposed system overcomes these limitations by enhancing material compatibility, transitional behavior, and software integration.

We used a pre-designed Triply Periodic Minimal Surface (TPMS) as input geometry in a compression test simulation in Fusion 360, applying a 50KN vertical load. The TPMS, created with the *Axolotl* plugin [75] in Grasshopper3D, features periodic undulations representing stress variations (Fig. 13a). Color gradients from blue (low stress) to yellow (high stress) indicate stress concentrations.

Three PLA filaments (yellow, blue, and green) were assigned to filament motors E1, E2, and E3, respectively. The G-code embeds material data, placing blue filament in low-stress areas, yellow in high-stress zones, and green in medium-stress regions. During printing, the blending auger (E0) maintains a constant speed, with filament feeds adjusting to stress magnitudes. The resulting multicolor TPMS print (Fig. 13c, d) accurately captures the model's stress distribution and intricate structure.

4. Discussion

This study introduces the Single-Nozzle Multi-Filament (SNMF) system as an advanced extrusion-based MMAM technology that supports gradient material compositions and transitions through active mixing. The design addresses three key objectives outlined in the introduction: establishing a robust single-nozzle multimaterial system, controlling material transitions with high fidelity, and providing advanced design strategies for complex multimaterial objects.

4.1. System design and performance

The SNMF system exhibits high controllability by integrating multiple materials feeds into a single nozzle with an active mixing auger, eliminating the need for nozzle switching. This single-nozzle approach simplifies the hardware and reduces potential points of failure, enabling seamless material transitions and allowing for real-time adjustments to the auger speed. The sys controllability allows for precise adjustment of material composition during transitions, making it adaptable to a variety of applications requiring specific material blends. It improves print efficiency by avoiding delays associated with nozzle switching in multi-nozzle systems. The continuous gradient and mixing capabilities enable high-quality transitions, making it suitable for applications needing both structural integrity and visual consistency. The sys reliance on viscosity-compatible materials limits the range of materials it can effectively handle. For materials with highly divergent viscosity, achieving a homogeneous mixture is challenging, potentially compromising bonding and structural performance. Additionally, while the single-nozzle design simplifies the system, it may struggle with rapid material changes due to the time required for thorough mixing in the auger, especially at lower speeds.

4.2. Material fidelity control

Material fidelity Control in the SNMF system is achieved by controlling gradient composition and understanding the material transitional behavior between different filaments. Our numerical method allows us to visualize the designed MM object accurately. While materializing the visualization, the rotational speed directly impacts the fidelity of material transitions, as it regulates the extent and smoothness of blending between materials. Lower auger speeds promote thorough mixing, resulting in stronger bonds and smoother gradients, while higher speeds allow for quicker transitions but may yield less cohesive gradients. This capability to adjust gradient composition enables users to balance fidelity and material bonding performance based on specific application requirements. The sys control over gradient composition and transitional material interface provides flexibility to optimize both the mechanical strength and visual quality of multimaterial prints. It allows for gradual transitions with optimal inter-material bonding. The ability to adjust gradient smoothness based on transitional behavior makes the SNMF system effective in scenarios where consistency in material properties and visual uniformity are critical. While lower active mixing speeds benefit gradient smoothness and bonding strength, they can potentially increase print times, which may not be ideal for applications that prioritize speed. Conversely, higher active mixing speeds may compromise transition quality, affecting bonding strength and potentially reducing durability. The SNMF sys material fidelity control over gradient composition and transitional material interface is optimized for materials with similar viscosity; this limits the system's versatility with more complex material combinations where viscosity differences could lead to less predictable transitional behavior.

4.3. Design and modeling strategies

The SNMF system employs advanced design strategies, including image sampling, discrete patches, and surface division, to support complex geometries and tailored material properties. These strategies enable efficient translation of CAD models into multimaterial, fabrication-ready objects, supporting intricate design realizations without post-processing. These strategies streamline the design-to-fabrication process, allowing for the versatile and efficient production of multimaterial objects directly from CAD models. By embedding specific material properties into the model, the SNMF system enhances both the functional and aesthetic characteristics of printed objects. This approach reduces the need for post-processing and assembly, which are often necessary in conventional MMAM systems, saving time and costs. The complexity of these strategies can increase computational

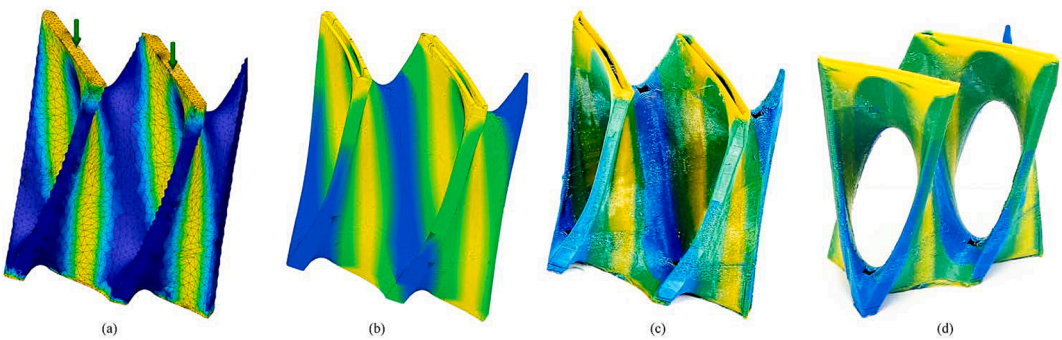

Fig. 13. A Triply Periodic Minimal Surface (TPMS) geometry printed with PLA filament of three colors based on the FEA result of two-point loading: (a) the loading condition and the FEA result; (b) the toolpath visualization with embedded material information, where yellow indicates higher stress; and (c) (d) the final print with high fidelity represents the FEA result. (For interpretation of the references to color in this figure legend, the reader is referred to the web version of this article.)

requirements, leading to longer design and slicing times, especially for intricate geometries. Additionally, while the design strategies support material gradient control, they are limited by the sys material compatibility, as the SNMF performs best with viscosity-matched materials. This restricts the system's application in scenarios requiring extreme material property contrasts within a single object.

4.4. Future directions

Future work on the SNMF system could enhance system design and performance by broadening material compatibility, increasing transition speed, and incorporating multi-axis printing. Expanding the range of compatible viscosity would open new applications, while optimized auger design or adaptive speed controls could enable faster material changes without sacrificing bond quality. Adding multi-axis movement would also support complex geometries, improving both strength and flexibility in multimaterial prints.

For material fidelity control, future efforts should focus on dynamic algorithms to adjust auger speed and feed rate for precise gradient control. Enhanced control at the material interface could enable smoother transitions between materials with dissimilar viscosity, possibly through localized heating or surface modifications. Predictive modeling of material behavior could further improve fidelity, allowing for accurate, consistent transitions while reducing setup time.

In design and modeling strategies, efforts to optimize computational efficiency could speed up the transition from CAD to print-ready models. Improved embedding of material properties in designs would enable gradient-based and stress-specific material distributions. Extending the sys capacity to handle extreme material contrasts, such as flexible-to-rigid or conductive-to-insulative transitions, would also expand its applicability across diverse multimaterial printing needs.

5. Conclusion

This study presents a single-nozzle multi-filament printing system compatible with various filaments and capable of active mixing, which enables smooth transitions and gradient multimaterial compositions. By detailing both the technical and methodological aspects, this work expands the understanding of MMAM (multimaterial additive manufacturing), offering a complete workflow from design to fabrication. The slicing method integrates material information directly into G-Code, enhancing fidelity in MMAM processes. Addressing a material fidelity gap in MMAM, this work introduces a numerical model and active mixing control for the SNMF system to manage precise material transitions and gradient compositions within complex multimaterial objects. The ability to control material placement with high accuracy enables a more seamless and integrated design process, supporting intricate designs with controlled material properties. Through case studies, the SNMF system demonstrates versatility in various printing scenar image sampling for intricate 2D patterns, discrete patches for function-specific structures, and surface division for continuous geometries. These applications showcase the sys capacity to produce complex, functional, multimaterial objects, such as a compressive column with added non-load-bearing material.

The study establishes an alternative MMAM framework with higher fidelity capabilities, though further refinements in the blending mechanism, material compatibility, and scalability are needed. Future developments aim to integrate robotic arms and scalable extrusion systems, positioning the SNMF system as a robust platform for multimaterial object design and production across disciplines.

CRediT authorship contribution statement

Teng Teng: Writing – review & editing, Writing – original draft, Validation, Software, Project administration, Methodology, Investigation, Formal analysis, Data curation, Conceptualization. **Yefan Zhi:** Formal analysis, Methodology, Software, Visualization, Writing – original draft, Writing – review & editing. **Masoud Akbarzadeh:** Conceptualization, Funding acquisition, Resources, Supervision, Validation, Writing – review & editing.

Funding

This research was supported by the National Science Foundation Future Eco Manufacturing Research Grants NSF, FMRG-2037097 CMMI and NSF CAREER-1944691 CMMI and the Advanced Research Projects Agency–Energy (ARPA-E) Grant of the U.S. Department of Energy (DE-AR0001631) awarded to Dr. Masoud Akbarzadeh.

Declaration of competing interest

The authors declare the following financial interests/personal relationships which may be considered as potential competing interests: Masoud Akbarzadeh reports financial support was provided by National Science Foundation Future Eco Manufacturing Research Grants NSF, FMRG-2037097 CMMI and NSF CAREER-1944691 CMMI and the Advanced Research Projects Agency–Energy (ARPA-E) Grant of the U.S. Department of Energy (DE-AR0001631). Teng Teng, Yefan Zhi, Masoud Akbarzade has patent SINGLE-NOZZLE MULTI-FILAMENT (SNMF) SYSTEM FOR FUSED DEPOSITION MODELING PRINTER SYSTEMS pending to The Trustees of the University of Pennsylvania. If there are other authors, they declare that they have no known competing financial interests or personal relationships that could have appeared to influence the work reported in this paper.

Acknowledgements

The authors would like to acknowledge and thank the writing advice provided by Dr. Maximilian E. Ororbia.

The authors would also like to acknowledge and thank Dr. Kun-hao Yu for the content suggestions.

Appendix A. Supplementary data

Supplementary data to this article can be found online at https://doi.org/10.1016/j.matdes.2024.113479.

Data availability

The authors confirm that the data supporting the findings of this study are available within the article and its Supplementary Materials.

References

[1] E. MacDonald, R. Wicker, Multiprocess 3d printing for increasing component functionality, *Science* 353 (6307) (2016) aaf2093.
[2] S. Torquato, "Heterogeneous materials: a paradigm for interdisciplinary research article," *Complex Materials Theory Group*, 1997.
[3] V. Kumar, D. Dutta, An approach to modeling & representation of heterogeneous objects, *J. Mech. Des.* 150 (1998) 659.
[4] A. Nazir, O. Gokcekaya, K.M.M. Billah, O. Ertugrul, J. Jiang, J. Sun, S. Hussain, Multi-material additive manufacturing: a systematic review of design, properties, applications, challenges, and 3d printing of materials and cellular metamaterials, *Mater. Des.* (2023) 111661.
[5] Y. Li, Z. Feng, L. Hao, L. Huang, C. Xin, Y. Wang, E. Bilotti, K. Essa, H. Zhang, Z. Li, F. Yan, T. Peijs, A review on functionally graded materials and structures via additive manufacturing: from multi-scale design to versatile functional properties, Adv. Mater. Technol. 5 (6) (2020) 1900981, https://doi.org/10.1002/admt.201900981.
[6] M. Rafiee, R.D. Farahani, D. Therriault, Multi-material 3d and 4d printing: a survey, Adv. Sci. 7 (12) (2020) 1902307, https://doi.org/10.1002/advs.201902307.
[7] R.F. Gibson, A review of recent research on mechanics of multifunctional composite materials and structures, *Compos. Struct.* 92 (12) (2010) 2793–2810.
[8] J. Feng, J. Fu, Z. Lin, C. Shang, B. Li, A review of the design methods of complex topology structures for 3d printing, *Visual Comput. Ind. Biomed. Art* 1 (1) (2018) 1–16.

[9] S. Belhabib, S. Guessasma, Compression performance of hollow structures: from topology optimisation to design 3d printing, *Int. J. Mech. Sci.* 133 (2017) 728–739.
[10] Y. Feng, T. Yamada, Multi-material topology optimization for additive manufacturing considering maximum build volume and assembly process, *Eng. Anal. Bound. Elem.* 163 (2024) 616–640.
[11] X. Huang, S. Su, Z. Xu, Q. Miao, W. Li, L. Wang, Advanced composite materials for structure strengthening and resilience improvement, *Buildings* 13 (10) (2023) 2406.
[12] L. Lopes, A. Silva, O. Carneiro, Multi-material 3d printing: the relevance of materials affinity on the boundary interface performance, *Addit. Manuf.* 23 (2018) 45–52.
[13] A. Darnal, Z. Shahid, H. Deshpande, J. Kim, A. Muliana, Tuning mechanical properties of 3d printed composites with pla: Tpu programmable filaments, *Compos. Struct.* 318 (2023) 117075.
[14] A. Dutto, M. Zanini, E. Jeoffroy, E. Tervoort, S.A. Mhatre, Z.B. Seibold, M. Bechthold, A.R. Studart, 3d printing of hierarchical porous ceramics for thermal insulation and evaporative cooling, *Adv. Mater. Technol.* 8 (4) (2023) 2201109.
[15] M.H. Ali, N. Mir-Nasiri, W.L. Ko, Multi-nozzle extrusion system for 3d printer and its control mechanism, *Int. J. Adv. Manuf. Technol.* 86 (2016) 999–1010.
[16] S. Khalil, J. Nam, A. Darling, W. Sun, Multi-nozzle biopolymer deposition for freeform fabrication of tissue constructs. In *2004 International Solid Freeform Fabrication Symposium*, 2004.
[17] M.A. Skylar-Scott, J. Mueller, C.W. Visser, J.A. Lewis, Voxelated soft matter via multimaterial multinozzle 3d printing, *Nature* 575 (7782) (2019) 330–335.
[18] J. Yin, C. Lu, J. Fu, Y. Huang, Y. Zheng, Interfacial bonding during multi-material fused deposition modeling (fdm) process due to inter-molecular diffusion, *Mater. Des.* 150 (2018) 104–112.
[19] A. Inamdar, M. Magana, F. Medina, Y. Grajeda, R. Wicker, Development of an automated multiple material stereolithography machine. In *2006 International Solid Freeform Fabrication Symposium*, 2006.
[20] E. Sodupe-Ortega, A. Sanz-Garcia, A. Pernia-Espinoza, C. Escobedo-Lucea, Accurate calibration in multi-material 3d bioprinting for tissue engineering, *Materials* 11 (8) (2018) 1402.
[21] D.B. Kolesky, R.L. Truby, A.S. Gladman, T.A. Busbee, K.A. Homan, J.A. Lewis, 3d bioprinting of vascularized, heterogeneous cell-laden tissue constructs, *Adv. Mater.* 26 (19) (2014) 3124–3130.
[22] L. Serex, A. Bertsch, P. Renaud, Microfluidics: A new layer of control for extrusion-based 3d printing, *Micromachines* 9 (2) (2018) 86.
[23] M. Costantini, S. Testa, P. Mozetic, A. Barbetta, C. Fuoco, E. Fornetti, F. Tamiro, S. Bernardini, J. Jaroszewicz, W. Świe˛szkowski, et al., Microfluidic-enhanced 3d bioprinting of aligned myoblast-laden hydrogels leads to functionally organized myofibers in vitro and in vivo, *Biomaterials* 131 (2017) 98–110.
[24] H. Zhao, Y. Chen, L. Shao, M. Xie, J. Nie, J. Qiu, P. Zhao, H. Ramezani, J. Fu, H. Ouyang, et al., Airflow-assisted 3d bioprinting of human heterogeneous microspheroidal organoids with microfluidic nozzle, *Small* 14 (39) (2018) 1802630.
[25] X. Li, J.M. Zhang, X. Yi, Z. Huang, P. Lv, H. Duan, Multimaterial microfluidic 3d printing of textured composites with liquid inclusions, *Adv. Sci.* 6 (3) (2019) 1800730.
[26] J.O. Hardin, T.J. Ober, A.D. Valentine, J.A. Lewis, Microfluidic printheads for multimaterial 3d printing of viscoelastic inks, *Adv. Mater.* 27 (21) (2015) 3279–3284.
[27] W. Liu, Y.S. Zhang, M.A. Heinrich, F. De Ferrari, H.L. Jang, S.M. Bakht, M. M. Alvarez, J. Yang, Y.-C. Li, G. Trujillo-de Santiago, et al., Rapid continuous multimaterial extrusion bioprinting, *Adv. Mater.* 29 (3) (2017) 1604630.
[28] J.O. Hardin, T.J. Ober, A.D. Valentine, J.A. Lewis, 3d printing: microfluidic printheads for multimaterial 3d printing of viscoelastic inks (adv. mater. 21/2015), *Adv. Mater.* 27 (21) (2015) 3278.
[29] D. Baca, R. Ahmad, The impact on the mechanical properties of multi-material polymers fabricated with a single mixing nozzle and multi-nozzle systems via fused deposition modeling, *Int. J. Adv. Manuf. Technol.* 106 (9–10) (2020) 4509–4520.
[30] H. Song, J. Martínez, P. Bedell, N. Vennin, S. Lefebvre, Colored fused filament fabrication, *ACM Trans. Graph. (TOG)* 38 (5) (2019) 1–11.
[31] F. Fenollosa, R. Uceda, A. Tejo, L. Calvo, L. Poudelet, I. Buj, Research on Desktop 3d Printing Multi-Material New Concepts vol. 1193 (2021) 012043.
[32] T. Cameron, E. Naseri, B. MacCallum, A. Ahmadi, Development of a disposable single-nozzle printhead for 3d bioprinting of continuous multi-material constructs, *Micromachines* 11 (5) (2020) 459.
[33] Z. Tian, Q. Zhong, H. Zhang, T. Yin, J. Zhao, G. Liu, Y. Zhao, H.N. Li, Y. He, Optimising printing fidelity of the single-nozzle based multimaterial direct ink writing for 3d food printing, *Virtual Phys. Prototyping* 19 (1) (2024) e2352075.
[34] C.P. Lee, M.J.Y. Ng, N.M.Y. Chian, M. Hashimoto, Multi-material direct ink writing 3d food printing using multi-channel nozzle, *Future Foods* 10 (2024) 100376.
[35] V. Hessel, H. Löwe, F. Schönfeld, Micromixers—a review on passive and active mixing principles, *Chem. Eng. Science* 60 (8–9) (2005) 2479–2501.
[36] H.E. Meijer, M.K. Singh, T.G. Kang, J.M. Den Toonder, P.D. Anderson, Passive and active mixing in microfluidic devices, in: *Macromolecular Symposia*, vol. 279, Wiley Online Library, 2009, pp. 201–209.
[37] H. Lan, "Active mixing nozzle for multi-material and multi-scale 3d printing," in *International Manufacturing Science and Engineering Conference*, vol. 50732, p. V002T01A024, American Society of Mechanical Engineers, 2017.
[38] J.M. Ortega, M. Golobic, J.D. Sain, J.M. Lenhardt, A.S. Wu, S.E. Fisher, L.X. Perez Perez, A.W. Jaycox, J.E. Smay, E.B. Duoss, et al., Active mixing of disparate inks for multimaterial 3d printing, *Adv. Mater. Technol.* 4 (7) (2019) 1800717.
[39] A.M. Golobic, M.D. Durban, S.E. Fisher, M.D. Grapes, J.M. Ortega, C.M. Spadaccini, E.B. Duoss, A.E. Gash, K.T. Sullivan, Active mixing of reactive materials for 3d printing, *Adv. Eng. Mater.* 21 (8) (2019) 1900147.
[40] T.J. Ober, D. Foresti, J.A. Lewis, Active mixing of complex fluids at the microscale, *Proc. Natl. Acad. Sci.* 112 (40) (2015) 12293–12298.
[41] B. Duncan, R.D. Weeks, B. Barclay, D. Beck, P. Bluem, R. Rojas, M. Plaut, J. Russo, S.G. Uzel, J.A. Lewis, et al., Low-loss graded dielectrics via active mixing of nanocomposite inks during 3d printing, *Adv. Mater. Technol.* 8 (3) (2023) 2201496.
[42] I. Hassan, P.R. Selvaganapathy, Microfluidic printheads for highly switchable multimaterial 3d printing of soft materials, *Adv. Mater. Technol.* 7 (9) (2022) 2101709.
[43] Z.C. Kennedy, J.F. Christ, Printing polymer blends through in situ active mixing during fused filament fabrication, *Addit. Manuf.* 36 (2020) 101233.
[44] L. Jaksa, D. Pahr, G. Kronreif, A. Lorenz, Development of a multi-material 3d printer for functional anatomic models, Int. J. Bioprinting 7 (4) (2021).
[45] J.S. Pelz, N. Ku, W.T. Shoulders, M.A. Meyers, L.R. Vargas-Gonzalez, Multi-material additive manufacturing of functionally graded carbide ceramics via active, in-line mixing, *Addit. Manuf.* 37 (2021) 101647.
[46] D.J. Roach, C.M. Hamel, C.K. Dunn, M.V. Johnson, X. Kuang, H.J. Qi, The m4 3d printer: A multi-material multi-method additive manufacturing platform for future 3d printed structures, *Addit. Manuf.* 29 (2019) 100819.
[47] H.T. Afarani, N.H. Moser, E.J. Garboczi, E.N. Esfahani, J.J. Biernacki, Print fidelity metrics for additive manufacturing of cement-based materials, *Addit. Manuf.* 55 (2022) 102784.
[48] A. Schwab, R. Levato, M. D'Este, S. Piluso, D. Eglin, J. Malda, Printability and shape fidelity of bioinks in 3d bioprinting, *Chem. Rev.* 120 (19) (2020) 11028–11055.
[49] M.N. Islam, B. Boswell, A. Pramanik, An investigation of dimensional accuracy of parts produced by three-dimensional printing, in: In *Proceedings of the World Congress on Engineering 2013*, 2013, pp. 522–525.
[50] K. Tiwari, S. Kumar, Analysis of the factors affecting the dimensional accuracy of 3d printed products, *Mater. Today: Proc.* 5 (9) (2018) 18674–18680.
[51] A. Telea, A. Jalba, "Voxel-based assessment of printability of 3d shapes," in *Mathematical Morphology and Its Applications to Image and Signal Processing: 10th International Symposium, ISMM 2011, Verbania-Intra, Italy, July 6-8, 2011. Proceedings 10*, pp. 393–404, Springer, 2011.
[52] J.T. Green, I.A. Rybak, J.J. Slager, M. Lopez, Z. Chanoi, C.M. Stewart, R. V. Gonzalez, Local composition control using an active-mixing hotend in fused filament fabrication, *Addit. Manuf. Lett.* 7 (2023) 100177.
[53] W. Li, A.J. Martin, B. Kroehler, A. Henderson, T. Huang, J. Watts, G.E. Hilmas, M.C. Leu, "Fabricating functionally graded materials by ceramic on-demand extrusion with dynamic mixing," in *2018 International Solid Freeform Fabrication Symposium*, University of Texas at Austin, 2018.
[54] S.G. Uzel, R.D. Weeks, M. Eriksson, D. Kokkinis, J.A. Lewis, Multimaterial multinozzle adaptive 3d printing of soft materials, *Adv. Mater. Technol.* 7 (8) (2022) 2101710.
[55] A. Verma, A. Kapil, D. Klobčar, A. Sharma, A review on multiplicity in multi-material additive manufacturing: process, capability, scale, and structure, *Materials* 16 (15) (2023) 5246.
[56] A. Bandyopadhyay, B. Heer, Additive manufacturing of multi-material structures, *Mater. Sci. Eng.: R: Rep.* 129 (2018) 1–16.
[57] L. Yang, H. Miyanaji, D. Janaki Ram, A. Zandinejad, S. Zhang, Functionally Graded Ceramic Based Materials Using Additive Manufacturing: Review and Progress vol. 258 (2016) 43–55.
[58] A. Pajonk, A. Prieto, U. Blum, U. Knaack, Multi-material additive manufacturing in architecture and construction: a review, *J. Build. Eng.* 45 (2022) 103603.
[59] D. Qiu, N.A. Langrana, Void eliminating toolpath for extrusion-based multi-material layered manufacturing, *Rapid Prototyping J.* 8 (1) (2002) 38–45.
[60] S. Bhashyam, K. Hoon Shin, D. Dutta, An integrated cad system for design of heterogeneous objects, *Rapid Prototyping J.* 6 (2) (2000) 119–135.
[61] H. Wargnier, F. Kromm, M. Danis, Y. Brechet, Proposal for a multi-material design procedure, *Mater. Des. (1980–2015)* (56) (2014) 44–49.
[62] X. Yao, S.K. Moon, G. Bi, J. Wei, A multi-material part design framework in additive manufacturing, *Int. J. Adv. Manuf. Technol.* 99 (2018) 2111–2119.
[63] C. Wade, G. Williams, S. Connelly, B. Kopec, R. MacCurdy, Openvcad: An open source volumetric multi-material geometry compiler, *Addit. Manuf.* 79 (2024) 103912.
[64] R. Contributors, "Diamond hotend." https://reprap.org/wiki/Diamond_Hotend, 2018. Accessed: September 18, 2023.
[65] M. Bi, L. Xia, P. Tran, Z. Li, Q. Wan, L. Wang, W. Shen, G. Ma, Y. Xie, Continuous contour-zigzag hybrid toolpath for large format additive manufacturing, Addit. Manuf. 55 (2022) 102822.
[66] X. Chen, G. Fang, W.-H. Liao, C.C. Wang, Field-based toolpath generation for 3d printing continuous fibre reinforced thermoplastic composites, *Addit. Manuf.* 49 (2022) 102470.
[67] L. Xia, S. Lin, G. Ma, Stress-based tool-path planning methodology for fused filament fabrication, *Addit. Manuf.* 32 (2020) 101020.
[68] W. Chiu, S. Tan, Multiple material objects: from cad representation to data format for rapid prototyping, *Comput.-Aided Des.* 32 (12) (2000) 707–717.
[69] E. Brancewicz-Steinmetz, J. Sawicki, P. Byczkowska, The influence of 3d printing parameters on adhesion between polylactic acid (pla) and thermoplastic polyurethane (tpu), *Materials* 14 (21) (2021) 6464.
[70] N.P. Sorimpuk, W.H. Choong, B.-L. Chua, Thermoforming characteristics of pla/tpu multi-material specimens fabricated with fused deposition modelling under different temperatures, *Polymers* 14 (20) (2022) 4304.

[71] T. Teng, Y. Zhi, K.-H. Yu, S. Yang, M. Akbarzadeh, "Continuous multi-filament 3d printing for tension-compression structure components," in *Proceedings of IASS 2023 symposium Integration of Design and Fabrication*, (Melbourne, Australia), July 10-14 2023.
[72] S. Mozaffari, M. Akbarzadeh, T. Vogel, Graphic statics in a continuum: Strut-and-tie models for reinforced concrete, *Comput. Struct.* 240 (2020) 106335.
[73] M. Bolhassani, A.T. Ghomi, A. Nejur, M.O. Furkan, I. Bartoli, M. Akbarzadeh, "Structural behavior of a cast-in-place funicular polyhedral concrete: Applied 3d graphic statics," in *Proceedings of IASS Annual Symposia*, vol. 2018, p. 1–8, International Association for Shell and Spatial Structures (IASS), 2018.
[74] X. Peng, L. Yue, S. Liang, S. Montgomery, C. Lu, C.-M. Cheng, R. Beyah, R.R. Zhao, H.J. Qi, Multi-color 3d printing via single-vat grayscale digital light processing, *Adv. Funct. Mater.* 32 (28) (2022) 2112329.
[75] M. Bernhard, M. Hansmeyer, B. Dillenburger, "Volumetric modelling for 3d printed architecture," in *Advances in Architectural Geometry 2018*, (Göteborg, Sweden), pp. 392–415, 09 2018.